

Joint Trajectory and Resource Optimization for HAPs-SAR Systems with Energy-Aware Constraints

Bang Huang, *Member, IEEE*, Kihong Park, *Senior Member, IEEE*, Xiaowei Pang, Mohamed-Slim Alouini, *Fellow, IEEE*,

Abstract—This paper investigates the joint optimization of trajectory planning and resource allocation for a high-altitude platform stations synthetic aperture radar (HAPs-SAR) system. To support real-time sensing and conserve the limited energy budget of the HAPs, the proposed framework assumes that the acquired radar data are transmitted in real time to a ground base station for SAR image reconstruction. A dynamic trajectory model is developed, and the power consumption associated with radar sensing, data transmission, and circular flight is comprehensively analyzed. In addition, solar energy harvesting is considered to enhance system sustainability. An energy-aware mixed-integer nonlinear programming (MINLP) problem is formulated to maximize radar beam coverage while satisfying operational constraints. To solve this challenging problem, a sub-optimal successive convex approximation (SCA)-based framework is proposed, incorporating iterative optimization and finite search. Simulation results validate the convergence of the proposed algorithm and demonstrate its effectiveness in balancing SAR performance, communication reliability, and energy efficiency. A final SAR imaging simulation on a 9-target lattice scenario further confirms the practical feasibility of the proposed solution.

Index Terms—Communication, High-altitude platform stations (HAPs), mixed-integer nonlinear programming (MINLP), SAR, successive convex approximations (SCA).

I. INTRODUCTION

THE *Top 10 Emerging Technologies of 2024* report released by the *World Economic Forum (WEF)* highlights the transformative potential of high-altitude platform stations (HAPs) in extending wireless connectivity to regions underserved by conventional terrestrial and satellite infrastructure [1], [2]. As a key enabler of non-terrestrial networks (NTNs) [3], HAPs are increasingly regarded as a foundational technology for future wireless communication systems. Operating in the stratosphere at altitudes of 20–30 km, HAPs uniquely combine the broad-area coverage of satellites with the maneuverability and flexible deployment of unmanned aerial vehicles (UAVs), making them especially suitable for long-endurance missions such as persistent connectivity, environmental monitoring, and real-time observation.

Driven by the growing global demand for ubiquitous, high-throughput, and low-latency wireless services, HAPs are poised to play a pivotal role in the development of integrated satellite–airborne–terrestrial communication networks.

The authors are with the Computer, Electrical and Mathematical Science and Engineering (CEMSE) division in King Abdullah University of Science and Technology (KAUST), Thuwal 6900, Makkah Province, Saudi Arabia. (Emails: bang.huang@kaust.edu.sa; kihong.park@kaust.edu.sa; xiaowei.pang@kaust.edu.sa; slim.alouini@kaust.edu.sa.) (Corresponding author: Bang Huang)

Compared with conventional satellite constellations, HAPs offer several key advantages, including lower deployment costs, shorter deployment timelines, and significantly reduced communication latency [4]. These benefits have placed HAPs at the forefront of both academic research [5] and industrial innovation [6]–[8], reinforcing their strategic relevance in the evolution of next-generation wireless ecosystems.

Although the concept of HAPs has been around for nearly three decades [9]–[11], its large-scale deployment has long been constrained by technological limitations. Earlier efforts were hindered by low solar energy conversion efficiency, the absence of lightweight structural materials, and inadequate avionics and control capabilities. However, recent advances in enabling technologies—such as high-performance composite materials, high-efficiency solar energy systems, antenna beamforming, and autonomous avionics—have collectively revived momentum in HAPs development [5]. Depending on mission-specific requirements, such as payload, power demand, and coverage objectives, modern HAPs platforms can be realized in the form of balloons, airships, or fixed-wing solar-powered aircraft [12].

Recent works have proposed architectural visions and communication frameworks for future HAPs-based systems [13], while surveys and technology trend analyses have highlighted the maturity of airframe, power, and payload subsystems required for sustained high-altitude operations [2]. Large-scale stochastic-geometry analyses further show that directional HAPs beams can deliver reliable wide-area coverage even under dense spatial reuse [14]. Complementary cellular enhancements, such as two-tier terrestrial/HAPs architectures [15] and non-orthogonal multiple access (NOMA)-assisted remote-coverage schemes [16], underscore the role of HAPs in extending service to underserved regions.

Beyond radio access, the stratosphere is evolving into a compute continuum. Hierarchical aerial-edge frameworks now coordinate task off-loading, user association, and resource orchestration across cooperating UAVs and HAPs [17]–[19], while multi-HAPs clusters embedded in space–air–ground–sea (SAGS) networks reduce latency for maritime and polar users [18]. Physical-layer innovations reinforce this evolution. Laser relays that exploit Fresnel–Poincaré–Kummer optics for terrestrial-HAPs-satellite links [20], adaptive beam-switching protocols for high-speed rail [21], hemispherical antenna arrays that equalize capacity across footprints [22], reconfigurable intelligent surfaces (RIS)-assisted terahertz (THz) NTNs links [23], and multi-HAPs THz relays robust to I/Q imbalance [24] demonstrate the feasibility of ultra-high-capacity

stratospheric links, while optical inter-HAPs backbones boost reliability for integrated space-air-ground networks [25].

Sustainability threads permeate these advances. Energy-aware radio-access planning [26], data-centre-enabled HAPs concepts [27], and cloud-enabled HAPs delivering equitable 6G access [28] illustrate the shift toward carbon-neutral, service-oriented NTN. Power-allocation strategies for HAPs-assisted LEO backhauls [29], efficient data-transmission protocols for massive HAPs constellations [30], and joint user-association/beamforming designs in satellite-HAPs-ground networks [31] complete the picture of a maturing ecosystem in which HAPs evolve from simple airborne relays to fully integrated compute-and-sensing hubs orchestrating resources across the SAGS continuum.

HAPs combine cost-effective deployment with wide-area coverage, agile repositioning, and multi-month endurance, making them attractive not only for bridging the digital divide but also for mission-critical services such as disaster relief, environmental monitoring, and smart agriculture [12], [32]. Among the sensing modalities that can unlock these services, synthetic-aperture radar (SAR) is particularly compelling because it delivers high-resolution images day or night, in virtually any weather. After earthquakes, landslides, or floods, events that often coincide with heavy cloud cover or rain, SAR can rapidly map damage, track terrain deformation, and guide emergency response. Equipping HAPs with SAR sensors therefore provides a practical path to real-time, resilient situation awareness at continental scales. Recent work extends this concept even further. HAPs-assisted integrated sensing-and-communication (ISAC) architectures couple high-resolution surveillance with secure data delivery [33], while mission-oriented schedulers that coordinate satellites, HAPs, and ground nodes enable specialised applications ranging from oil-spill monitoring [34] to uninterrupted connectivity along high-speed-rail corridors [35].

Motivated by the need for an integrated design that simultaneously exploits the wide-area connectivity of HAPs and the all-weather, high-resolution sensing of SAR, this paper proposes a joint trajectory-and-resource optimization framework for HAPs-SAR missions. Moreover, the contributions of this paper can be summarized as follows:

- While most existing HAPs research has focused primarily on communication functions, this paper explicitly incorporates SAR imaging into the system model, an essential capability for applications such as disaster response, environmental monitoring, and smart agriculture. Recognizing the unique circular flight dynamics of HAPs platforms, we propose a novel dual-mode SAR sensing framework that integrates both small-circle circular SAR (CSAR) and large-circle circular trace scanning SAR (CTSSAR) modes. This hybrid configuration leverages the maneuvering flexibility of HAPs to enhance spatial coverage and imaging diversity. To the best of the authors' knowledge, this is the first work to introduce such a coordinated SAR sensing architecture tailored to the operational characteristics of stratospheric platforms.
- Building upon the proposed sensing architecture, this paper presents a mathematical formulation of the HAPs

trajectory, alongside an analytical characterization of the SAR sensing region and the necessary conditions for successful image acquisition. Given the stringent energy constraints inherent to stratospheric platforms, real-time onboard SAR processing is typically infeasible, necessitating the offloading of raw echo data to a ground base station (BS) for reconstruction. Accordingly, we also model the communication link required to support reliable and timely data transmission. From an energy perspective, the HAPs must judiciously allocate its limited solar-harvested power across three competing subsystems, propulsion, energy-intensive SAR payloads, and long-range data downlinks. To holistically capture these interdependent factors, we formulate a unified mixed-integer nonlinear programming (MINLP) framework that jointly optimizes flight trajectory, sensing performance, communication quality, and energy sustainability.

- To reconcile these constraints, we develop a successive convex approximation (SCA) algorithm augmented with a finite search over SAR sweeps. This hybrid solver yields iterative, tractable sub-problems whose solutions provably converge to a high-quality operating point.
- Comprehensive simulations confirm the effectiveness of the proposed approach. The HAPs adaptively adjusts altitude and heading to maximize radar coverage, which improves energy utilization, and sustains reliable data transmission for real-time, off-board image reconstruction. A final simulation over a 9-target lattice demonstrates accurate SAR imaging and validates the practical feasibility of the joint design.

The remainder of this paper is structured as follows. Section II introduces the system model, including the HAPs trajectory, SAR sensing geometry, communication link, and energy supply, all of which are mathematically characterized. In Section III, the joint optimization problem is formulated as a MINLP, and a solution approach is developed based on the SCA method. Section IV presents simulation results that validate the proposed framework. Finally, Section V concludes the paper and discusses future research directions.

II. SYSTEM MODEL

Fig.1 illustrates the schematic of the proposed SAR imaging framework for ground observation using a HAPs. The HAPs performs a circular flight around the vertical (z) axis and operates in two distinct SAR modes to balance resolution and coverage. As shown in Fig.1(a), the platform initially flies along a small-radius circular trajectory and performs CSAR imaging [36], which enables high-resolution, full-azimuth imaging of the target scene. To expand the sensing range, the platform gradually increases its flight radius, transitioning into the CTSSAR mode [37], as illustrated in Fig.1(b). This mode enables scene-wide mapping by scanning concentric circular rings.

Throughout the flight, SAR echo data is transmitted to nearby ground BS for real-time image reconstruction. This design avoids performing onboard SAR processing, which is generally infeasible due to the HAPs's limited energy

and computational resources. To ensure high-quality image acquisition, the CSAR mode requires that the radar beam fully illuminates the entire circular track, enabling full-perspective imaging. In contrast, the CTSSAR mode demands that each circular ring is fully covered to guarantee complete scene mapping. Additionally, to ensure seamless coverage over extended ground areas, it is essential that adjacent circular sweeps are contiguous, without any gaps between beam footprints.

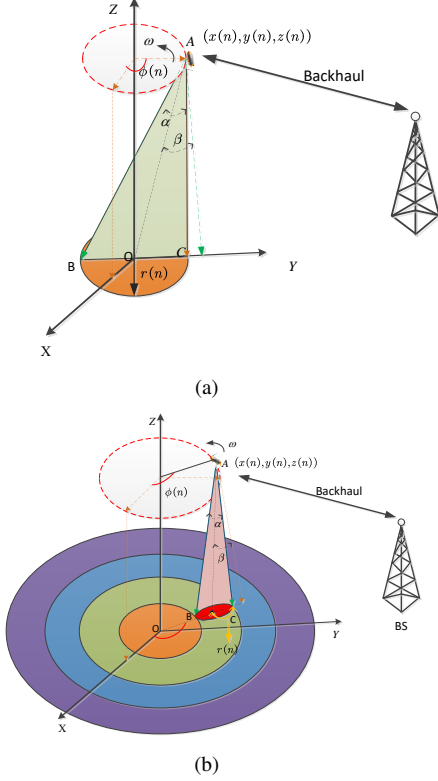


Fig. 1. Imaging scenario for HAPs-SAR with a backhaul communication link. (a) Circular SAR mode. (b) Circular Trace Scanning SAR mode.

A. Design Trajectory

Consider a HAPs operating above the ground and moving along a circular trajectory of radius R in a plane parallel to the xy plane. The platform rotates with a constant angular velocity denoted by ω . At the initial slow-time instant $\eta = 0$, the HAPs is assumed to be located on the positive side of the x -axis. Accordingly, the azimuth angle relative to the x -axis is given by $\varphi(\eta) = \omega\eta$. Let T represent the time required for the HAPs to complete one full circular revolution. This period is uniformly discretized into N time intervals, where the time step for each segment is defined as $\Delta = \frac{T}{N}$. To ensure consistent discretization, Δ should be selected such that $N = T/\Delta$ is an integer.

To complete the prescribed ground mapping strip, the HAPs is assumed to perform M full circular rotations. To more precisely characterize the temporal evolution of the HAPs trajectory over these circular sweeps, we define the following set of time slots:

$$\mathbb{A} = \{1, N + 1, \dots, (M - 1)N + 1\}, \quad (1)$$

and

$$\mathbb{B} = \{N, 2N, \dots, MN\}, \quad (2)$$

to represent the indices corresponding to the start and end time slots of each circular motion, respectively. Subsequently, define the set \mathbb{C} as

$$\begin{aligned} \mathbb{C} &= \{1, 2, \dots, NM\} \setminus \{\mathbb{A} \cup \mathbb{B}\} \\ &= \{n \in \{1, 2, \dots, NM\} \mid (n - 1) \bmod N \neq 0, n \bmod N \neq 0\} \end{aligned} \quad (3)$$

which corresponds to the indices of all remaining time intervals. The position of the HAPs at time slot n is represented as $(x(n), y(n), z(n))$ in the three-dimensional (3D) Cartesian coordinate system. Here, $x(n)$ and $y(n)$ represent the coordinates in the xy -plane, while $z(n)$ denotes the height of the HAPs above the ground.

The HAPs performs a circular motion around the z -axis, returning to the starting point along the x -axis. In other words, to ensure the completeness of the ground mapping strip, the HAPs must align the start and end points during each circular motion. It is important to note that the time indices in set \mathbb{A} typically correspond to the time slots in which the distance between the HAPs platform and the z -axis changes.

Further, the angle traversed by the HAPs at time slots n can be represented as

$$\phi(n) = 2\pi \frac{n-1}{N}, n \in \mathbb{A}, \quad (4)$$

$$\phi(n) = 2\pi \frac{n}{N}, n \in \mathbb{B}, \quad (5)$$

$$\phi(n) = \omega n \Delta, n \in \mathbb{C}, \quad (6)$$

where $n = 1, 2, \dots, MN$. (4)-(5) ensure that the start and end points of each circular motion coincide, while (6) guarantees that the HAPs performs circular motion.

Assume that the center of the SAR signal beam emitted by the HAPs forms an angle β with the vertical axis of the HAPs projected onto the xy plane. The width of the signal beam emitted by the HAPs is α . In this case, it is easy to determine that the distance from the center of the beam to the edge of the beam on the ground can be expressed as

$$r(n) = \frac{1}{2} z(n) (\tan \alpha_1 - \tan \alpha_2), \quad (7)$$

where the angles α_1 and α_2 are given by $\alpha_1 = \beta + \frac{\alpha}{2}$ and $\alpha_2 = \beta - \frac{\alpha}{2}$, respectively.

Furthermore, the 3D position coordinates of the HAPs at time slot n can be represented as

$$C1 : x(1) = z(1) \tan \beta, \quad (8)$$

$$C2 : x(n) = x(n-1) + 2r(n) + \dot{z}(n), \forall n \in \mathbb{A} \setminus \{1\}, \quad (9)$$

$$C3 : x(n) = x\left(\left(\left\lceil \frac{n}{N} \right\rceil - 1\right)N + 1\right) \cos(\varphi(n)), \forall n \in \mathbb{B} \cup \mathbb{C}, \quad (10)$$

$$C4 : y(n) = x\left(\left(\left\lceil \frac{n}{N} \right\rceil - 1\right)N + 1\right) \sin(\varphi(n)), \quad (11)$$

$$C5 : z(n) = z(n-1), \forall n \in \mathbb{B} \cup \mathbb{C}. \quad (12)$$

where $\lceil \cdot \rceil$ denotes the ceiling function and $\dot{z}(n) = [z(n) - z(n-1)] \tan \alpha_2$. The constraint $C2$ ensures there

are no gaps between the beam coverage areas of adjacent sweeps. Meanwhile, $C3$ and $C4$ ensure that the HAPs follows a circular trajectory.

B. SAR Analysis

This subsection will analyze the ground coverage area for SAR imaging using HAPs. Furthermore, when HAPs operates

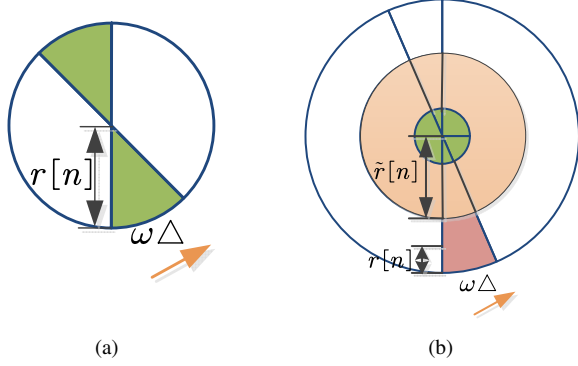


Fig. 2. Covering area for HAPs. (a) CSAR mode. (b) CTSSAR mode.

in CSAR mode, specifically mapping the smallest circle as shown in Fig. 2(a), it is straightforward to derive that the area covered by the SAR beam within each time interval Δ can be expressed as

$$S_1 = \omega \Delta r^2(n). \quad (13)$$

Fig. 2(b) shows the imaging results of the HAPs operating in CTSSAR mode for the ground surface. The area scanned by SAR within the time interval Δ can be calculated as

$$\begin{aligned} S_2 &= \frac{1}{2} [2r(n) + \tilde{r}(n)]^2 \omega \Delta - \frac{1}{2} \tilde{r}^2(n) \omega \Delta \\ &= 2 \{r^2(n) + r(n) \tilde{r}(n)\} \omega \Delta \end{aligned} \quad (14)$$

with expression of $\tilde{r}(n)$ is given by

$$\tilde{r}(n) = \begin{cases} r(n-N), & \lceil \frac{n}{N} \rceil = 2, \\ r(n-N) + \sum_{m=2}^{\lceil \frac{n}{N} \rceil - 1} 2r(n-mN), & \lceil \frac{n}{N} \rceil > 2. \end{cases} \quad (15)$$

Hence, the area observed by HAPs during the entire surveying period can be represented as

$$S = \sum_{n=2}^N S_1 + \sum_{n=N+1, n \notin \mathbb{A}}^{MN} S_2. \quad (16)$$

The preceding discussion has analyzed the entire imaging coverage area of the HAPs. Next, we will introduce two parameters in detail, the SAR data rate and the minimum signal-to-noise ratio (SNR) required to achieve effective SAR imaging. In this respect, based on the results from [38], [39], the data rate generated by SAR imaging in time slot n can be expressed as

$$D_{\min}(n) = B_w \left[\frac{2}{c} (R_{\text{far}}(n) - R_{\text{near}}(n)) + T_p \right] \cdot PRF \quad [\text{bit/s}], \quad (17)$$

where B_w represents the bandwidth of the SAR transmitted pulse, and T_p denotes the pulse width. The symbol c stands for the speed of light, and PRF refers to the pulse repetition frequency. $R_{\text{far}}(n)$ and $R_{\text{near}}(n)$ indicate the radar's maximum unambiguous range and minimum unambiguous range, respectively, which are given by

$$R_{\text{far}}(n) = \frac{z(n)}{\cos \alpha_1}, R_{\text{near}}(n) = \frac{z(n)}{\cos \alpha_2}. \quad (18)$$

Furthermore, based on the radar equation [40], the SNR received by the HAPs receiver is given by

$$\text{SNR}(n) = \frac{P_{\text{Rad}}(n) G_t G_r \lambda^3 \sigma_0 c T_p PRF}{256 \pi^3 R_0^3 K T F_n B_w L_s V(n) \sin \delta} \quad (19)$$

where $P_{\text{Rad}}(n)$ denotes the radar transmission power at the n -th time slot. G_t and G_r represent the transmit and receive gains, respectively. λ is the wavelength, while σ_0 signifies the backscatter coefficient. R_0 refers to the distance between the radar and the center of the scene, commonly known as the reference distance. K stands for Boltzmann's constant, and T represents the receiver temperature. F_n denotes the receiver noise, L_s indicates system loss, and $V(n)$ is platform velocity, whose expression is¹

$$C6: V(n) = \sqrt{x(n) g \tan \zeta}, \forall n \in \mathbb{A} \quad (20)$$

$$C7: V(n) = V(n-1), \forall n \in \mathbb{B} \cup \mathbb{C}. \quad (21)$$

Here, the definition of the symbol g is provided in Table II and ζ denotes the banking angle. Moreover, δ represents the beam incidence angle, the angle between the antenna line-of-sight vector and its intersection with the xy plane. In addition, the following relationship can be easily derived from Fig. 3, namely

$$\delta + \beta = \frac{\pi}{2}, z(n) = R_0 \sin \delta. \quad (22)$$

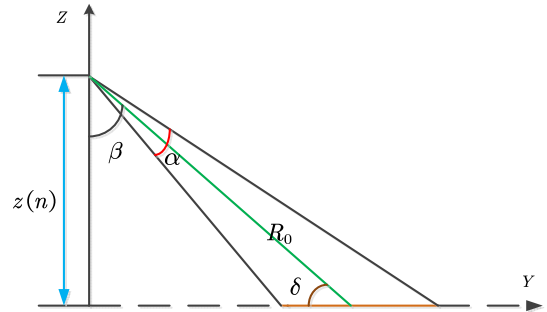


Fig. 3. Geometric schematic of the HAPs within the yz plane.

Moreover, inserting (22) into (19) yields

$$\text{SNR}(n) = \frac{P_{\text{Rad}}[n] G_t G_r \lambda^3 \sigma_0 c T_p PRF \cos^2 \beta}{256 \pi^3 z^3(n) K T F_n B_w L_s V(n)}. \quad (23)$$

¹The velocity expression in (20) is derived solely based on the equilibrium between centrifugal and gravitational forces. This formulation remains valid under the assumption that complex factors such as wind disturbances, lift variations, and other aerodynamic effects are neglected [41], [42].

C. Communication Link

HAPs platforms are expected to primarily rely on renewable energy sources, such as solar or wind power, for their long-term energy supply [2]. Given the limited onboard power and processing capabilities, real-time SAR image reconstruction directly on the HAPs is generally infeasible. Instead, the raw ground-scattered SAR echoes must be transmitted to a ground BS for post-processing. This requirement establishes a data backhaul link between the HAPs and the BS.

To conserve onboard storage and support real-time ground-based imaging, it is crucial that the SAR echo data should be transmitted promptly to the BS, rather than accumulated and sent only after the entire mapping operation is complete. This subsection analyzes the characteristics of this air-to-ground communication link.

For modeling purposes, we assume that the HAPs-to-BS backhaul link consists solely of a line-of-sight (LOS) channel, and the air-to-ground propagation adheres to a free-space path loss model. The channel power gain at time slot n is then expressed as

$$\rho(n) = \frac{\rho_0}{d^2(n)}. \quad (24)$$

Here, ρ_0 denotes the channel gain at a reference distance of 1m, while $d(n)$ represents the LOS distance between the HAPs and the BS at time slot n . Assuming the BS is positioned at (x_s, y_s, z_s) in a 3D Cartesian coordinate system, the expression for $d(n)$ can be written as

$$d(n) = \sqrt{(x(n) - x_s)^2 + (y(n) - y_s)^2 + (z(n) - z_s)^2}. \quad (25)$$

If the SAR's transmitted communication power at time slot n is denoted as $P_{\text{Com}}(n)$, the received SNR at the BS can be expressed as

$$\gamma(n) = \frac{P_{\text{Com}}(n) \rho(n)}{\sigma_0^2} \quad (26)$$

with σ_0^2 denoting the receiver's noise power. Furthermore, based on the above analysis, the instantaneous backhaul throughput from the HAPs to the BS can be readily given by

$$D_c(n) = B_c \log(1 + \gamma(n)) \quad (27)$$

where B_c represents the bandwidth of communicating signal. To enable the real-time transmission of SAR sensing data, the following condition must be satisfied

$$C8 : D_c(n) > D_{\min}(n). \quad (28)$$

The reason for using $>$ instead of \geq in C8 is that this paper does not account for essential signals, such as clock synchronization and the positional information of the HAPs, which are transmitted alongside the SAR raw echo.

D. Energy Analysis

The proposed HAPs concept involves operating at higher stratospheric altitudes during daylight hours, serving as an airborne BS for ground-based communication while simultaneously performing sensing tasks by receiving echo signals from the surface. During flight, the HAPs is equipped with solar

panels to continuously harvest solar energy, which powers its real-time operations, such as propulsion and data transmission, and stores surplus energy to support nighttime activity.

In typical communication-only configurations, a HAPs may remain quasi-static during nighttime to minimize energy consumption. However, when sensing is included, the platform must remain fully operational 24/7. This requirement is particularly important in emergency scenarios, such as earthquakes, where the HAPs must perform real-time SAR imaging over disaster-stricken areas and immediately transmit sensing data to the ground BS. Such real-time capabilities are essential for enabling timely and accurate decision-making by rescue teams.

In this respect, based on the findings of [43], the propulsion power necessary to ensure that the HAPs maintains stable circular motion at time slot n can be expressed as

$$P_{\text{Mot}}(n) = \frac{1}{\cos^2(\zeta) \eta_p \eta_e} \left[\frac{1}{2} \rho(z(n)) V^3(n) \tilde{S} C + \varepsilon \frac{2W^2}{\rho(z(n)) \tilde{S} V(n)} \right] \quad (29)$$

where η_p, η_e represent the efficiencies of propeller and engine, respectively. Meanwhile, \tilde{S} and W are the total area of the wing and the weight of HAPs, respectively. The Zero-lift drag is defined by C and the expression of coefficient is $\varepsilon = 1/(\pi e R_w)$ with e and R_w being the Oswald's efficiency factor [44] and wing aspect ratio [45], respectively. Besides, $\rho(z(n))$ is the air density at an altitude $z(n)$, given by

$$\rho(z(n)) = \frac{p_h(z(n))}{R_s T_p(z(n))} \quad (30)$$

with the expressions of $p_h(z(n))$ and $T_p(z(n))$ [46] being

$$p_h(z(n)) = p_{b1} \left(\frac{T_b}{T_b + L_b(z(n) - H_1)} \right)^{\frac{gM}{RL_b}}, H_1 \leq z(n) \leq H_2 \quad (31)$$

and

$$T_p(z(n)) = T_b + L_b(z(n) - H_1), H_1 \leq z(n) \leq H_2 \quad (32)$$

Here, all used symbols in (30) and (31) are summarized in Table II.

TABLE I
SYMBOLS USED IN (30) AND (31)

Symbol	Explanation	Value	Unit
p_{b1}	base static pressures	5474.889	Pa
g	gravitational acceleration	9.8	m/s ²
M	molar mass of Earth's air	0.0289644	kg/mol
T_b	base temperature	216.65	K
L_b	base temperature lapse rate	6.7	K/km
R	universal gas constant	8.31432	N · m/mol · K
R_s	specific gas constant	287.052	J/kg · K
H_1	height (lower limit)	20	km
H_2	height (upper limit)	32	km

Therefore, we can model the combined energy requirements for maintaining the HAPs platform's operations across its propulsion system, radar sensing capabilities, and communication tasks in the given time slot n , as

$$P_{\text{Total}}(n) = P_{\text{Mot}}(n) + P_{\text{Rad}}(n) + P_{\text{Com}}(n). \quad (33)$$

Next, we proceed to analyze the solar power $P_{\text{Har}}(n)$ harvested by the solar panels of HAPs. Drawing upon the findings presented in [47], [48], the expression for $P_{\text{Har}}(n)$ can be elegantly derived as²

$$P_{\text{Har}}(n) = \eta_h AI(z(n)) \quad (34)$$

where the symbol η_h denotes the energy conversion efficiency of the solar panel and A is the effective solar energy collection area of the solar panel. $I(z(n))$ represents the solar radiation intensity per unit area, which depends on factors such as the season, date/time, geographical location, and the operational altitude of the HAPs. However, this paper primarily investigates the impact of varying flight altitudes on $I(z(n))$, disregarding the influences of observer geographical latitude, solar declination, and local hour angle [47] on radiation intensity. Hence, based on the above analysis and the conclusions from [43], [47], [48], an approximate expression for $I(z(n))$ can be given by

$$I(z(n)) = I_0 \exp\{-p_R(z(n))\alpha_{\text{int}}\}. \quad (35)$$

Here, I_0 represents the standard solar constant at zero air mass, with a value of 1367 W/m². The extinction coefficient, denoted as $\alpha_{\text{int}} = 0.32$, represents the attenuation of light in clear sky conditions. This value is indicative of the combined effects of scattering and absorption by atmospheric molecules and aerosols under standard clear-sky scenarios. Moreover, The parameter $p_R(z(n))$ is defined as the ratio between the atmospheric pressure at a given altitude $z(n)$ and the pressure at ground level. It quantifies the relative pressure at altitude $z(n)$ compared to the ground, and is expressed as $p_R(z(n)) = \frac{p_h(z(n))}{p_0}$. Here, $p_h(z(n))$ is the pressure at altitude $z(n)$ and p_0 is the pressure at ground level, whose value is 101325Pa.

Based on the above analysis, we can easily deduce that the remaining power in time slot n , after accounting for the power $P_{\text{Har}}(n)$ obtained from solar energy, the power required to maintain HAPs aerodynamics $P_{\text{Mot}}(n)$, the power used for radar sensing $P_{\text{Rad}}(n)$, and the power used for communication back to the BS $P_{\text{Com}}(n)$, can be expressed as

$$\begin{aligned} P_{\text{Re}}(n) &= P_{\text{Har}}(n) - P_{\text{Total}}(n) \\ &= P_{\text{Har}}(n) - P_{\text{Mot}}(n) - P_{\text{Rad}}(n) - P_{\text{Com}}(n). \end{aligned} \quad (36)$$

The variation in the battery energy carried by the HAPs from time slot $n-1$ to time slot n can be formulated as

$$C9: E(n) = E(n-1) + \eta_a P_{\text{Re}}(n)\Delta, \forall n \neq 1 \quad (37)$$

where the parameter η_a is defined by

$$\eta_a = \begin{cases} \eta_b, P_{\text{Re}}(n) > 0 \\ \eta_c, P_{\text{Re}}(n) \leq 0 \end{cases} \quad (38)$$

with η_b and η_c representing the efficiencies of battery charging and discharging, respectively.

Constraint $C9$ defines the energy allocation framework for the HAPs system, ensuring that energy usage remains within sustainable limits while maximizing overall system performance under available power constraints.

²Nighttime operation implies zero energy harvesting, i.e., $P_{\text{Har}}(n) = 0$, which is not considered in this paper.

III. TRAJECTORY AND RESOURCE ALLOCATION OPTIMIZATION

In this section, we first formulate the problem of maximizing the SAR-sensed ground area S , subject to the HAPs trajectory and resource allocation constraints. We then develop a tractable solution approach based on SCA to address this optimization problem.

A. Objective Formulation

The objective of this paper is to maximize the SAR ground coverage while satisfying the constraints associated with radar sensing, data transmission, and HAPs mobility. To this end, we jointly optimize the HAPs trajectory parameters, denoted by $\{z, N\}$, and the power allocation variables, denoted by $\{P_{\text{Mot}}, P_{\text{Rad}}, P_{\text{Com}}, E\}$. Specifically, $z = \{z(n)\}$ represents the altitude profile of the HAPs, while $P_{\text{Mot}}, P_{\text{Rad}}, P_{\text{Com}}$, and $E = \{E(n)\}$ denote the time-varying power allocated for mobility, radar sensing, communication, and the remaining onboard energy, respectively, for each time slot n . Based on these definitions, the overall optimization problem can be formulated as

$$\begin{aligned} (P1) : & \max_{z, N, P_{\text{Mot}}, P_{\text{Rad}}, P_{\text{Com}}, E} S \\ \text{s.t.} & C1 - C9 \\ & C10: P_{\text{Rad}}(n) = P_{\text{Rad}}(n-1), n \in \{\mathbb{A}\} \setminus \{1\}, \\ & C11: 0 \leq P_{\text{Rad}}(n) \leq P_{\text{Rad}}^{\text{max}}, 0 \leq P_{\text{Com}}(n) \leq P_{\text{Com}}^{\text{max}}, \forall n, \\ & C12: \text{SNR}(n) > \text{SNR}_{\text{min}}, \forall n, \\ & C13: E(1) = E_{\text{Ini}}, \\ & C14: E(n) > 0, \forall n \neq 1, \\ & C15: z_{\text{min}} \leq z(n) \leq z_{\text{max}}, n \in \mathbb{A}, \\ & C16: V_{\text{min}} \leq V(n) \leq V_{\text{max}}, \forall n. \end{aligned} \quad (39)$$

Constraints $C1-C5$ define the motion trajectory of the HAPs, while $C6$ and $C7$ give the definition of the speed for the HAPs at time index. $C8$ ensures seamless and real-time transmission of the SAR raw data collected by the HAPs to the BS. The energy limitation of HAPs is encapsulated by constraint $C9$. Constraint $C10$ specifies that the radar's transmitted power remains constant at each moment, ensuring consistency in the radar's operational output. Constraint $C11$ indicates that the transmission power of both radar and communication systems must be non-negative and not exceed their respective maximum allowable transmission powers. Constraint $C12$ ensures that the echo SNR(n) at the HAPs satisfies the minimum SNR threshold required for successful imaging, denoted as SNR_{min} . Constraints $C13$ and $C14$ characterize the energy levels of the HAPs at the initial moment and at time n , respectively. $C15$ and $C16$ represent the operational altitude of HAPs and the speed limit of HAPs, respectively. It is important to note that z_{min} , z_{max} , and V_{max} are fixed constants, whereas V_{min} denotes the stalling speed, requiring HAPs to sustain a speed no lower than this threshold at the current altitude $z(n)$ to ensure adequate lift for steady-level flight. Its expression is given by $V_{\text{min}} = \sqrt{\frac{2W}{p_h(z(n))SC_L^{\text{max}}}}$, where C_L^{max} denotes the maximum lift coefficient.

The problem (P1) is a joint non-convex MINLP problem under the given optimization parameters. While the integer constraint on N does not directly affect the objective function, it influences the dimensionality of other parameters. Consequently, N cannot be optimized jointly with the other parameters. Therefore, the non-convex problem (P1), involving the integer variable $N \in \mathbb{N}$, is difficult to solve. In light of this, this paper proposes a suboptimal solution based on SCA to address problem (P1).

B. Solution for the Built Problem

By fixing the variable N in the first step, we can optimize the problem (P1). In this respect, for a given N , (P2) can be reformulated as

$$(P2) : \max_{z, P_{\text{Mot}}, P_{\text{Rad}}, P_{\text{Com}}, P_{\text{Har}}, \mathbf{E}} S \quad (40)$$

s.t. $C1 - C16$.

Even with N fixed, the presence of constraints C8, C9 and C12, continues to render (P2) a non-convex problem. To address the non-convexity of problem (P2), we adopt the SCA technique to transform it into a tractable sub-optimal convex problem. Furthermore, by proving that the variable N resides in a finite search space, the optimal value of N can be efficiently determined via exhaustive search.

We begin by reformulating constraint C8 into a convex form. Subsequently, it can be further simplified and equivalently rewritten as

$$C8 : \left(\mathbf{b}2^{\mathbf{a}z(n)} - 1 \right) \left[(x(n) - x_s)^2 + (y(n) - y_s)^2 + (z(n) - z_s)^2 \right] < \frac{\rho_0}{\sigma_0^2} P_{\text{Com}}(n), \forall n, \quad (41)$$

with $\mathbf{a} = \frac{2B_w P_{\text{RRF}}}{cB_c} \left(\frac{1}{\cos \alpha_1} - \frac{1}{\cos \alpha_2} \right)$ and $\mathbf{b} = 2^{\frac{B_w T_p P_{\text{RRF}}}{B_c}}$ being all positive.

Denote

$$h_1(x(n), z(n)) = \left(\mathbf{b}2^{\mathbf{a}z(n)} - 1 \right) (x(n) - x_s)^2, \quad (42)$$

$$h_2(y(n), z(n)) = \left(\mathbf{b}2^{\mathbf{a}z(n)} - 1 \right) (y(n) - y_s)^2, \quad (43)$$

$$h_3(z(n)) = \left(\mathbf{b}2^{\mathbf{a}z(n)} - 1 \right) (z(n) - z_s)^2. \quad (44)$$

Hence, (41) can be rewritten as

$$C8 : h_1(x(n), z(n)) + h_2(y(n), z(n)) + h_3(z(n)) < \frac{\rho_0}{\sigma_0^2} P_{\text{Com}}(n), \forall n. \quad (45)$$

Through the analysis of the Hessian matrix of the function $h_1(x(n), z(n))$, it can be concluded that $h_1(x(n), z(n))$ is not a convex function. However, we find that $h_1(x(n), z(n))$ can be expressed as the difference of convex functions (DC decomposition). Specifically, we have

$$h_1(x(n), z(n)) = \frac{1}{2} [g_1(z(n)) + g_2(x(n))]^2 - \frac{1}{2} [g_1^2(z(n)) + g_2^2(x(n))], \quad (46)$$

with $g_1(z(n)) = \mathbf{b}2^{\mathbf{a}z(n)} - 1$, $g_2(x(n)) = (x(n) - x_s)^2$. Note that $g_1(z(n))$ and $g_2(x(n))$ are both convex functions.

Building upon this, by employing the first-order Taylor expansion, the approximate representations of $g_1^2(z(n))$, $g_2^2(x(n))$ around point $\{x^k(n), y^k(n), z^k(n)\}$ are derived as

$$g_1^2(z(n)) \approx g_1^2(z^k(n)) + [g_1^2(z^k(n))]' [z(n) - z^k(n)], \quad (47)$$

$$g_2^2(x(n)) \approx g_2^2(x^k(n)) + [g_2^2(x^k(n))]' [x(n) - x^k(n)]. \quad (48)$$

Here, the superscript $(\cdot)'$ signifies the operation of computing the first derivative of a function.

Similarly, we have

$$h_2(y(n), z(n)) = \frac{1}{2} [g_1(z(n)) + g_3(y(n))]^2 - \frac{1}{2} [g_1^2(z(n)) + g_3^2(y(n))], \quad (49)$$

$$h_3(z(n)) = \frac{1}{2} [g_1(z(n)) + g_4(z(n))]^2 - \frac{1}{2} [g_1^2(z(n)) + g_4^2(z(n))] \quad (50)$$

where $g_3(y(n)) = (y(n) - y_s)^2$ and $g_4(z(n)) = (z(n) - z_s)^2$. Moreover, the first-order Taylor expansions of $g_3(y(n))$ and $g_4(z(n))$ around the point $\{x^k(n), y^k(n), z^k(n)\}$ can be elegantly given by

$$g_3^2(y(n)) \approx g_3^2(y^k(n)) + [g_3^2(y^k(n))]' [y(n) - y^k(n)], \quad (51)$$

$$g_4^2(z(n)) \approx g_4^2(z^k(n)) + [g_4^2(z^k(n))]' [z(n) - z^k(n)]. \quad (52)$$

Inserting (46)-(52) into (45) results in

$$\sum_{i=2}^4 [g_1(\varsigma_i) + g_i(\varsigma_i)]^2 - 3 [g_1^2(\varsigma_i^k) + [g_1^2(\varsigma_i^k)]' (\varsigma_i - \varsigma_i^k)] - \sum_{i=2}^4 \left\{ g_i^2(\varsigma_i^k) + [g_i^2(\varsigma_i^k)]' (\varsigma_i - \varsigma_i^k) \right\} < \frac{2\rho_0}{\sigma_0^2} P_{\text{Com}}(n), \forall n \quad (53)$$

with $\varsigma_2 = x(n)$, $\varsigma_3 = y(n)$ and $\varsigma_4 = z(n)$. To further streamline the resolution of the optimization problem (P2), this paper introduces three slack vectors, $\mathbf{p} = [p(1), p(2), \dots, p(MN)]^T \in \mathbb{R}^{MN}$, $\mathbf{q} = [q(1), q(2), \dots, q(MN)]^T \in \mathbb{R}^{MN}$ and $\mathbf{r} = [r(1), r(2), \dots, r(MN)]^T \in \mathbb{R}^{MN}$, at this juncture. Namely, the constraint C8 can be reformulated as

$$\widetilde{C8} : p^2(n) + q^2(n) + r^2(n) - 3 [g_1^2(\varsigma_4^k) + [g_1^2(\varsigma_4^k)]' (\varsigma_4 - \varsigma_4^k)] - \sum_{i=2}^4 \left\{ g_i^2(\varsigma_i^k) + [g_i^2(\varsigma_i^k)]' (\varsigma_i - \varsigma_i^k) \right\} < \frac{2\rho_0}{\sigma_0^2} P_{\text{Com}}(n), \forall n, \quad (54)$$

$$\widetilde{C8a} : g_1(z(n)) + g_2(x(n)) \leq p(n), \forall n, \quad (55)$$

$$\widetilde{C8b} : g_1(z(n)) + g_3(y(n)) \leq q(n), \forall n, \quad (56)$$

$$\widetilde{C8c} : g_1(z(n)) + g_4(z(n)) \leq r(n), \forall n. \quad (57)$$

Now, the subproblem (P2) can thus be approximated as the following optimization problem

$$(P3) : \begin{aligned} & \max_{z, P_{\text{Mot}}, P_{\text{Rad}}, P_{\text{Com}}, P_{\text{Har}}, \mathbf{E}} S \\ \text{s.t. } & C1 - C7, \widetilde{C8}, \widetilde{C8a}, \widetilde{C8b}, \widetilde{C8c}, C9 - C16. \end{aligned} \quad (58)$$

Note that problem (P3) remains non-convex due to the presence of constraints C9 and C12. In the following, we focus on addressing the non-convexity introduced by constraint C9. Accordingly, constraint C9 can be equivalently reformulated as:

$$\begin{aligned} \widetilde{C9} : P_{\text{Mot}}(n) - P_{\text{Har}}(n) &= \frac{E(n-1)}{\Delta\eta_a} \\ &- \frac{E(n)}{\Delta\eta_a} - P_{\text{Rad}}(n) - P_{\text{Com}}(n), \forall n \neq 1. \end{aligned} \quad (59)$$

At this stage, our attention can be directed toward $P_{\text{Mot}}(n)$. Accordingly, define

$$h_4(z(n), V(n)) = \frac{1}{2 \cos^2(\zeta) \eta_p \eta_e} \rho(z(n)) V^3(n) SC, \quad (60)$$

$$h_5(z(n), V(n)) = \frac{2\varepsilon W^2}{\cos^2(\zeta) \eta_p \eta_e \rho(z(n)) SV(n)}. \quad (61)$$

Furthermore, utilizing the results [43] clearly reveals that $h_4(z(n), V(n))$ and $h_5(z(n), V(n))$ are jointly nonconvex functions with respect to $z(n)$ and $V(n)$, respectively. Nevertheless, both $h_4(z(n), V(n))$ and $h_5(z(n), V(n))$ can be reformulated within the framework of DC programming, that is

$$\begin{aligned} h_4(z(n), V(n)) &= \frac{1}{2} [g_5(z(n)) + g_6(V(n))]^2 \\ &- \frac{1}{2} [g_5^2(z(n)) + g_6^2(V(n))], \end{aligned} \quad (62)$$

$$\begin{aligned} h_5(z(n), V(n)) &= \frac{1}{2} [g_7(z(n)) + g_8(V(n))]^2 \\ &- \frac{1}{2} [g_7^2(z(n)) + g_8^2(V(n))] \end{aligned} \quad (63)$$

where $g_5(z(n)) = \rho(z(n))$, $g_6(V(n)) = \frac{SCV^3(n)}{2 \cos^2(\zeta) \eta_p \eta_e}$, $g_7(z(n)) = \frac{1}{\rho(z(n))}$ and $g_8(V(n)) = \frac{2\varepsilon W^2}{\cos^2(\zeta) \eta_p \eta_e SV(n)}$. As demonstrated in Appendix A of [43], the functions $g_5(z(n))$, $g_6(V(n))$, $g_7(z(n))$, and $g_8(V(n))$ are all proven to be convex. Furthermore, by applying a first-order Taylor expansion, the functions $g_5(z(n))$, $g_6(V(n))$, $g_7(z(n))$, and $g_8(V(n))$ can be locally linearized around the point $(z^k(n), V^k(n))$, as

$$g_i^2(v_i) \approx g_i^2(v_i^k) + [g_i^2(v_i^k)]' [v_i - v_i^k], i = 5, 6, 7, 8, \quad (64)$$

with $v_5 = v_7 = z(n)$ and $v_6 = v_8 = V(n)$.

Subsequently, inserting (62)-(64) into (59) gives

$$\begin{aligned} \widetilde{C9} : & \frac{1}{2} [t^2(n) + u^2(n)] - P_{\text{Har}}(n) + P_{\text{Rad}}(n) \\ &- \frac{1}{2} \sum_{i=5}^8 [g_i^2(v_i^k) + [g_i^2(v_i^k)]' [v_i - v_i^k]] \\ &\leq \frac{E(n-1)}{\Delta\eta_a} - \frac{E(n)}{\Delta\eta_a} - P_{\text{Com}}(n), \forall n \neq 1. \end{aligned} \quad (65)$$

Here, $t(n)$ and $u(n)$ are components of the slack vectors $\mathbf{t} = [t(1), t(2), \dots, t(MN)]^T \in \mathbb{R}^{MN}$ and $\mathbf{u} = [u(1), u(2), \dots, u(MN)]^T \in \mathbb{R}^{MN}$. It is important to emphasize that \mathbf{t} and \mathbf{u} serve as slack variables introduced to enhance the tractability of the optimization problem (P3), and they are subject to

$$\widetilde{C9a} : g_5(z(n)) + g_6(V(n)) \leq t(n), \quad (66)$$

$$\widetilde{C9b} : g_7(z(n)) + g_8(V(n)) \leq u(n). \quad (67)$$

Therefore, the optimization problem (P3) can be approximated as

$$(P4) : \begin{aligned} & \max_{z, P_{\text{Mot}}, P_{\text{Rad}}, P_{\text{Com}}, P_{\text{Har}}, \mathbf{E}} S \\ \text{s.t. } & C1 - C7, \widetilde{C8}, \widetilde{C8a}, \widetilde{C8b}, \widetilde{C8c}, \\ & \widetilde{C9}, \widetilde{C9a}, \widetilde{C9b}, C10 - C16. \end{aligned} \quad (68)$$

It is worth noting that constraint C12 renders the optimization problem (P4) non-convex. In this regard, our primary focus is on reformulating constraint C12 into a convex form to facilitate efficient optimization. Specifically, because the constraint C12 involves a cubic polynomial in the HAPs altitude z , we can employ second-order cone programming (SOCP) to reformulate C12 accordingly. Hence, two slack variables $\varphi(n), \psi(n)$ are introduced here in vectors $\boldsymbol{\varphi} = [\varphi(1), \dots, \varphi(MN)]^T \in \mathbb{R}^{MN \times 1}$ and $\boldsymbol{\psi} = [\psi(1), \dots, \psi(MN)]^T \in \mathbb{R}^{MN \times 1}$ to rewrite the constraint C12 as [49]

$$\exists \varphi(n) \geq 0 \in \mathbb{R}, \widetilde{C12a} : \begin{bmatrix} \varphi(n) & z(n) \\ z(n) & 1 \end{bmatrix} \succeq \mathbf{0}, \forall n \quad (69)$$

$$\exists \psi(n) \geq 0 \in \mathbb{R}, \widetilde{C12b} : \begin{bmatrix} \psi(n) & \varphi(n) \\ \varphi(n) & z(n) \end{bmatrix} \succeq \mathbf{0}, \forall n \quad (70)$$

$$\widetilde{C12c} : \begin{bmatrix} P_{\text{Rad}}[n] \text{ con.} & V(n) \\ \psi(n) & 1 \end{bmatrix} \succeq \mathbf{0}, \forall n \quad (71)$$

where the symbol con. denoting the constant, whose expression is $\text{con.} = \frac{G_t G_r \lambda^3 \sigma_0 c T_p \text{PRF} \cos^2 \beta}{256 \pi^3 K T F_n B_w L_s \text{SNR}_{\min}}$.

As a result of the aforementioned transformations, the subproblem (P1) can be equivalently reformulated into a convex optimization problem, denoted as (P5), namely

$$(P5) : \begin{aligned} & \max_{z, P_{\text{Mot}}, P_{\text{Rad}}, P_{\text{Com}}, P_{\text{Har}}, \mathbf{E}} S \\ \text{s.t. } & C1 - C7, \widetilde{C8}, \widetilde{C8a}, \widetilde{C8b}, \widetilde{C8c}, \\ & \widetilde{C9}, \widetilde{C9a}, \widetilde{C9b}, C10 - C11, \\ & \widetilde{C12a}, \widetilde{C12b}, \widetilde{C12c}, C13 - C16. \end{aligned} \quad (72)$$

C. Method for optimal Number N^*

To tackle Problem (P1), we proceed in two steps. First, we solve sub-problem (P5) for every admissible fixed value of N . Next, from the resulting solutions we select the smallest N that still attains the maximum coverage area, thereby minimizing energy consumption. We can now invoke the following proposition to rigorously demonstrate that N admits only a finite number of feasible values. Consequently, the optimal N^* can be efficiently determined by performing a finite search.

Proposition 1. *The sweep N is subject to an upper bound.*

Proof. By leveraging constraint $C11$, a lower bound for the right-hand side of constraint $\widetilde{C9}$ can readily be established as

$$P_{\text{Mot}}(n) - P_{\text{Har}}(n) \leq \frac{E(n-1)}{\Delta\eta_a} - \frac{E(n)}{\Delta\eta_a}, \forall n \neq 1. \quad (73)$$

Subsequently, by summing both sides of the inequality, gives

$$\sum_{n=2}^{NM} [P_{\text{Mot}}(n) - P_{\text{Har}}(n)] \leq \sum_{n=2}^{NM} \left[\frac{E(n-1)}{\Delta\eta_a} - \frac{E(n)}{\Delta\eta_a} \right]. \quad (74)$$

Observing (74), the expression on the right-hand side can be rewritten as

$$\sum_{n=2}^{NM} \left[\frac{E(n-1)}{\Delta\eta_a} - \frac{E(n)}{\Delta\eta_a} \right] = \frac{E(1)}{\Delta\eta_a} - \frac{E(NM)}{\Delta\eta_a}. \quad (75)$$

Inserting (75) into (74) results in

$$\sum_{n=2}^{NM} [P_{\text{Mot}}(n) - P_{\text{Har}}(n)] \leq \frac{E(1)}{\Delta\eta_a} - \frac{E(NM)}{\Delta\eta_a} \leq \frac{E_{\text{Ini}}}{\Delta\eta_a}. \quad (76)$$

It is worth noting that during each sweep, the altitude and velocity remain constant, leading to fixed values for both power consumption and energy harvesting. Accordingly, we can readily derive³

$$N \leq \frac{E_{\text{Ini}}}{\Delta\eta_a \sum_{m=1}^M [P_{\text{Mot}}(m) - P_{\text{Har}}(m)]}. \quad (77)$$

(77) suggests that a feasible upper bound for N can be determined by solving for the minimum value of $\sum_{m=1}^M [P_{\text{Mot}}(m) - P_{\text{Har}}(m)]$. Hence, we can build the following problem, as

$$\begin{aligned} (P6) : & \min_{z(m), V(m), \tilde{t}} \tilde{t} \\ \text{s.t. } & C15 : z_{\min} \leq z(m) \leq z_{\max}, \\ & C16 : V_{\min} \leq V(m) \leq V_{\max}, \\ & C17 : \sum_{m=1}^M [P_{\text{Mot}}(m) - P_{\text{Har}}(m)] \leq \tilde{t}. \end{aligned} \quad (78)$$

The non-convexity of problem (P6) arises from the presence of constraint C17. To tackle this challenge, we adopt the SCA method, as previously employed. In this manner, problem

(P6) can be equivalently reformulated into the following convex problem (P7)

$$\begin{aligned} (P7) : & \min_{z(m), V(m), \tilde{t}} \tilde{t} \\ \text{s.t. } & \widetilde{C9a}, \widetilde{C9b}, C15, C16, \\ & \widetilde{C17} : \sum_{m=1}^M \left[\frac{1}{2} [t^2(m) + u^2(m)] - P_{\text{Har}}(m) \right. \\ & \left. - \frac{1}{2} \sum_{i=5}^8 [g_i^2(v_i^k) + [g_i^2(v_i^k)]' [v_i - v_i^k]] \right] \leq \tilde{t} \end{aligned} \quad (79)$$

An upper bound for the sweep number N can be further determined by solving the optimization problem (P7). Thus, the proposition is proved. \square

To address problem (P1), the SCA method is employed to iteratively solve the subproblems (P5) and (P7), as outlined in Algorithm 1. Both subproblems can be efficiently handled using the conventional solvers, for example the CVX [50].

Algorithm 1 Overall Optimization Framework Based on SCA

- 1: **Initialization:** $k = 1$, and the initial point $(z^1, \mathbf{V}^1) \in \mathbb{R}^{M \times 2}$, obtain the upper bound N^1 by solving (P7) around the point (z^1, \mathbf{V}^1) , $\xi_1 = \infty$, $\xi_2 = \infty$, **Set** tolerance δ_1, δ_2
 - 2: **while** $\xi_1 \geq \delta_1$ **do**
 - 3: Set $k = k + 1$
 - 4: Get the upper bound N^k and solutions (z^k, \mathbf{V}^k) by solving (P7) around the point $(z^{k-1}, \mathbf{V}^{k-1})$
 - 5: Update $\xi_1 = \left\lfloor \frac{N^k - N^{k-1}}{N^k} \right\rfloor$
 - 6: **end while**
 - 7: **Set** $N^{up} = N^k$, $S^* = -\infty$
 - 8: **for** $N = 1$ to N^{up} **do**
 - 9: Set $k = 1$, and the initial point $(x^1, y^1, z^1, \mathbf{V}^1) \in \mathbb{R}^{N \times 4}$, calculate the coverage S^1 by solving (P5) around the point $(x^1, y^1, z^1, \mathbf{V}^1) \in \mathbb{R}^{N \times 4}$
 - 10: **repeat**
 - 11: Set $k = k + 1$
 - 12: Get the coverage S^k and solutions $(x, y, z, \mathbf{V}, P_{\text{Mot}}, P_{\text{Rad}}, P_{\text{Com}}, P_{\text{Har}}, \mathbf{E})$ by solving (P5) around the point $(x^{k-1}, y^{k-1}, z^{k-1}, \mathbf{V}^{k-1})$
 - 13: Set $(x^k, y^k, z^k, \mathbf{V}^k) = (x, y, z, \mathbf{V})$
 - 14: Compute $\xi_2 = \left\lfloor \frac{S^k - S^{k-1}}{S^k} \right\rfloor$
 - 15: **until** $\xi_2 \leq \delta_2$
 - 16: Set $\xi_2 = \infty$
 - 17: **if** $S^k > S^*$ **then**
 - 18: Set $S^* = S^k$
 - 19: Set $(x^*, y^*, z^*, \mathbf{V}^*, P_{\text{Mot}}^*, P_{\text{Rad}}^*, P_{\text{Com}}^*, P_{\text{Har}}^*, \mathbf{E}^*) = (x^k, y^k, z^k, \mathbf{V}^k, P_{\text{Mot}}^k, P_{\text{Rad}}^k, P_{\text{Com}}^k, P_{\text{Har}}^k, \mathbf{E}^k)$
 - 20: **end if**
 - 21: **end for**
 - 22: **return** $S^*, (x^*, y^*, z^*, \mathbf{V}^*, P_{\text{Mot}}^*, P_{\text{Rad}}^*, P_{\text{Com}}^*, P_{\text{Har}}^*, \mathbf{E}^*)$
-

³The validity of (77) is based on the condition that the energy consumed for propulsion exceeds the energy harvested by the solar panels. This condition is practically reasonable, particularly during periods of low solar irradiance, such as early morning or late evening.

IV. SIMULATION RESULTS

In this section, we employ numerical simulations to rigorously validate the proposed approach, focusing on three-dimensional HAPs trajectory planning, resource allocation, and algorithm convergence. Unless otherwise specified, the system parameters are listed in Table II.

TABLE II
SYSTEM PARAMETERS

Parameter	Value	Parameter	Value
M	3	f	2GHz
G_t	20dB	G_r	20dB
T_p	10^{-6}	PRF	1000
B_w	100MHz	B_c	100MHz
(x_s, y_s, z_s)	(0, 0, 0)	α	15°
β	25°	$P_{\text{Rad}}^{\text{max}}$	46dBm
$P_{\text{Com}}^{\text{max}}$	40dBm	SNR_{min}	-10dB

To the best of the authors' knowledge, this work represents the first attempt to jointly investigate resource allocation and trajectory optimization for HAPs-enabled SAR systems. Due to the absence of established benchmark schemes in the existing literature, we construct two baseline approaches to facilitate comparative performance evaluation, in line with the practices adopted in related works [51]:

Benchmark 1: The radar transmit power is fixed to the optimal value obtained from the proposed method. Under this setting, problem (P5) is re-solved to determine the corresponding benchmark performance.

Benchmark 2: The communication transmit power is fixed to the optimal value derived from the proposed algorithm. With this assumption, problem (P5) is re-optimized to obtain Benchmark 2.

Fig. 4 presents the convergence behavior of Algorithm 1, where Figs. 4(a) and 4(b) illustrate the convergence trajectories corresponding to optimization problems (P7) and (P5), respectively. Since the optimization over N involves a finite search, it suffices to demonstrate the convergence of (P7) and (P5) to ensure the convergence of Algorithm 1. The results clearly indicate that the proposed algorithm converges rapidly, confirming the efficiency and effectiveness of the proposed optimization framework.

Fig. 5 illustrates the optimized three-dimensional trajectory of the HAPs, where the red arrows denote its flight direction and the magenta marker at the origin represents the ground BS location. The resulting trajectory configuration is governed by the trajectory constraints $C1-C4$, while the altitude variations arise from the sweep-wise adaptability permitted under constraint $C5$. From a system design perspective, although higher altitudes allow for broader beam coverage, they also incur significantly greater energy consumption. Despite the incorporation of solar energy harvesting via solar panels, the HAPs platform faces stringent energy limitations due to the substantial energy demands associated with sustained operation. As a result, it is not feasible for the HAPs to continuously operate at maximum altitude throughout the mission. Therefore, an adaptive altitude strategy is essential, balancing between extended coverage area and energy efficiency. The derived trajectory reflects a trade-off that maximizes SAR cov-

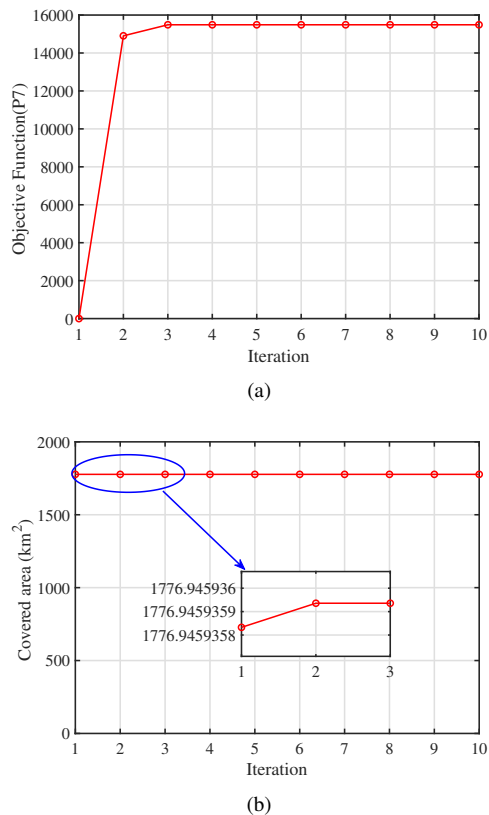


Fig. 4. Convergence of algorithm 1. (a) Convergence of Problem (P7), (b) Convergence of Problem (P5).

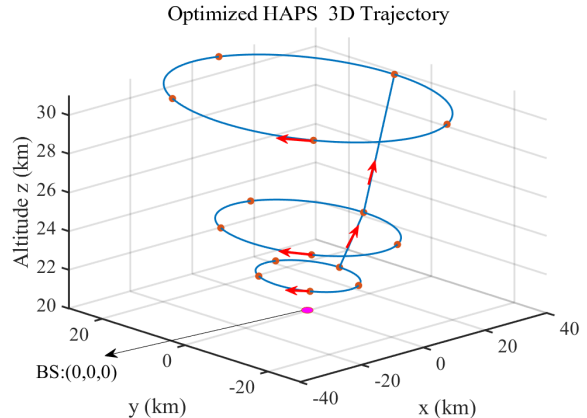


Fig. 5. Optimized HAPS-SAR 3D trajectory.

erage while ensuring operational sustainability under energy constraints.

Fig. 6 illustrates the communication power allocation under different BS deployment scenarios. The analysis reveals that as the HAPs ascends, increased communication power is necessary to satisfy constraint $C8$, which governs the minimum required data rate. This is attributed to the augmented path loss associated with higher altitudes, necessitating greater transmission power to maintain link quality. When the radar transmission power is fixed at its optimized value, the communication power can be further refined through optimization,

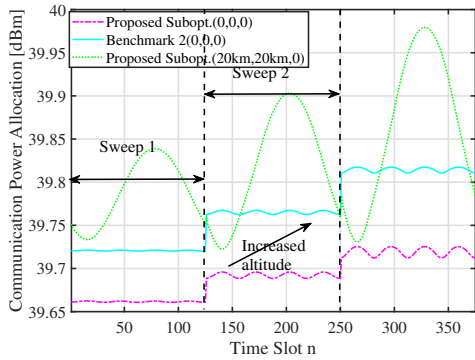


Fig. 6. Communication power allocation vs the time slot n .

as indicated by the blue solid line. Furthermore, when the BS is positioned at $(20\text{km}, 20\text{km}, 0)$, the communication power exhibits more pronounced temporal variations across time slots compared to the case where the BS is located at the origin $(0, 0, 0)$, as shown by the green dashed line. This behavior arises from the dynamic distance changes between the HAPs and the BS due to the HAPs's circular trajectory. To maintain the required communication rate under varying distances, the HAPs must adapt its transmission power accordingly. Additionally, the symmetry of the HAPs's circular motion imparts a corresponding symmetry to the communication power profile within a single sweep. This symmetry arises because the HAPs's distance to the BS varies in a predictable manner during its circular trajectory, leading to a mirrored pattern in the required communication power over time. These observations underscore the critical importance of adaptive power control strategies in HAPs operations. By dynamically adjusting communication power in response to altitude changes and BS positioning, it is possible to enhance energy efficiency and maintain robust communication links throughout the mission.

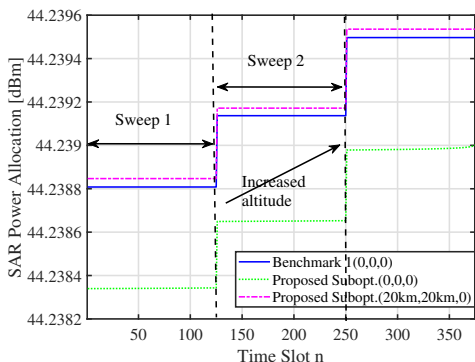


Fig. 7. SAR power allocation vs the time slot n .

Fig. 7 illustrates the SAR power allocation as a function of the time slot index. Unlike the communication power, which varies dynamically, the SAR transmission power remains constant within each sweep due to the enforcement of constraint $C10$. This constraint ensures that the radar system operates with uniform power across individual sweeps, maintaining

consistency in SAR illumination. Nonetheless, a similar trend is observed with respect to altitude. Namely as the HAPs ascends, the SAR system requires higher transmission power to ensure sufficient ground coverage and signal strength, owing to increased propagation losses at higher altitudes, which can be more clearly in (23). Furthermore, the location of the ground BS indirectly influences SAR power allocation. Variations in communication power, driven by the BS position and its associated rate constraints $C8$, can impose limitations on the total available power budget, thereby affecting the power allocated to SAR operations. This dependency is reflected by the magenta dashed line in the figure, highlighting the interplay between communication demands and radar resource allocation.

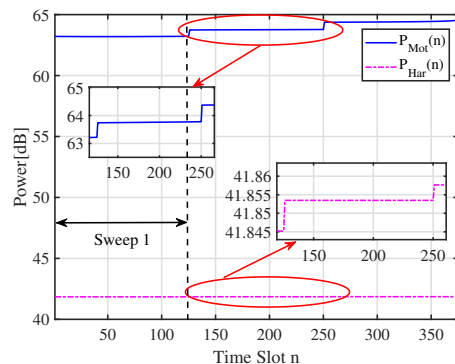


Fig. 8. Motion and harvesting power allocation.

Fig. 8 illustrates the temporal profiles of both the power consumed for maintaining HAPs mobility and the power harvested via onboard solar panels. Under the parameter configuration adopted in this paper, it is evident that the energy consumption consistently exceeds the harvested energy. This is primarily due to the analytical focus on the discharge phase of the solar-powered system, wherein the solar batteries are assumed to be fully charged, allowing for an isolated assessment of the HAPs-SAR system performance under energy depletion conditions. Although this paper focuses on the energy-limited operation scenario, it is important to acknowledge that in practical deployments, the HAPs must also harvest sufficient energy to sustain prolonged operation. Future investigations may explore joint charging and operational strategies to ensure system sustainability, as discussed in [16], [43]. Furthermore, it can be observed that within each sweep, the energy harvested and the energy consumed for propulsion are balanced. This is a direct consequence of constraints $C5-C7$, which enforce an energy neutrality condition over each sweep. Additionally, as the HAPs altitude increases, both the propulsion energy consumption and solar energy harvesting rise, driven respectively by increased aerodynamic resistance and enhanced solar irradiance at higher altitudes.

Fig. 9 presents the ratio of the remaining energy to the initial energy of the HAPs at each time slot n . Although the remaining energy reaches zero upon completion of the prescribed sensing mission, which is mathematically permissible, this condition is impractical for real-world systems. In practice,

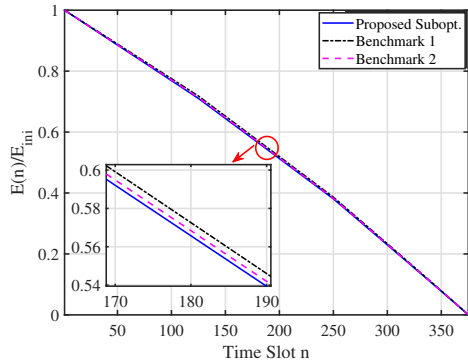


Fig. 9. Ratio of remaining energy to initial energy over time for the HAPs.

the HAPs must retain sufficient energy to either return to base or remain in standby mode for future tasks. Nevertheless, since this paper focuses solely on the discharging process and only requires satisfaction of constraint $C14$, the results depicted in Fig. 9 are considered feasible within the context of the proposed model. Furthermore, it is evident that the energy ratio decreases approximately linearly over time, with proposed method exhibiting the most rapid energy consumption among the compared schemes.

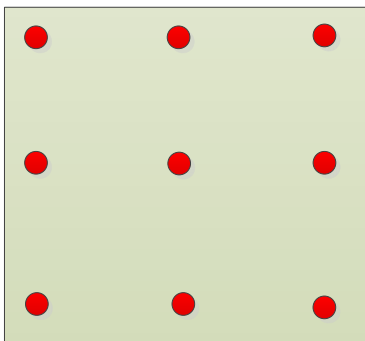


Fig. 10. SAR imaging scenario with a 9-target lattice configuration.

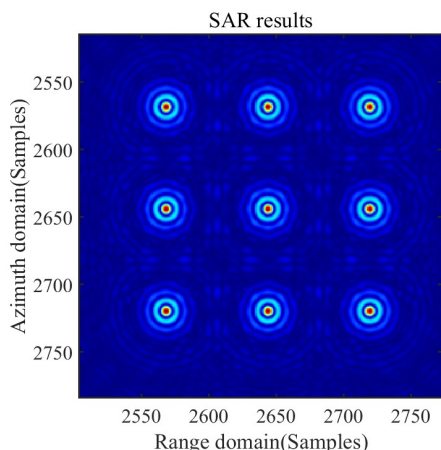


Fig. 11. SAR imaging results corresponding to the 9-target configuration.

To further verify the feasibility of the proposed trajectory and resource allocation strategy for SAR imaging, a simulation was conducted on the 9-target lattice scenario depicted in Fig. 10, using the parameters outlined in this paper and a well-established polar formatting algorithm (PFA) [36], [52], [53]. The corresponding imaging results are shown in Fig. 11. It can be clearly seen that all targets, both in the center of the scene and in the periphery, are accurately focused. These results provide additional evidence supporting the effectiveness of the proposed optimization framework.

V. CONCLUSION

In this work, we proposed a joint trajectory and resource optimization framework for HAPs-SAR systems aimed at real-time sensing and energy efficiency. By offloading SAR image reconstruction to a ground BS, the HAPs can operate with reduced onboard processing and energy costs. We developed a detailed flight model and performed energy analysis considering solar power harvesting and consumption from radar sensing, communication, and motion. A MINLP problem was formulated to maximize beam coverage under system constraints, and an SCA-based sub-optimal solution was proposed. Extensive simulations verified the convergence and effectiveness of the proposed algorithm across multiple performance dimensions. The SAR imaging results for a 9-target lattice scenario further validated the practicality and robustness of the optimization framework. Future work may extend this framework to include adaptive scheduling, multi-HAPs cooperative scenarios, and validation using real-world measurement data.

REFERENCES

- [1] World Economic Forum, "Top 10 Emerging Technologies of 2024," <https://www.weforum.org/publications/top-10-emerging-technologies-2024/>, 2024, accessed: 2025-05-10.
- [2] B. E. Y. Belmekki, A. J. Aljohani, S. A. Althubaity, A. A. Harthi, K. Bean, A. Aijaz, and M.-S. Alouini, "Cellular network from the sky: Toward people-centered smart communities," *IEEE Open Journal of the Communications Society*, vol. 5, pp. 1916–1936, 2024.
- [3] O. Anicho, P. Charlesworth, G. Baicher, A. Nagar *et al.*, "Multi-haps network implementation within 3GPP's NTN framework for 5G and beyond," *International Journal of Information, Communication Technology and Applications*, vol. 7, no. 1, pp. 7–12, 2021.
- [4] Y. Shibata, N. Kanazawa, K. Hoshino, Y. Ohta, and A. Nagate, "A study on cell configuration for HAPS mobile communications," in *2019 IEEE 89th Vehicular Technology Conference (VTC2019-Spring)*, Kuala Lumpur, Malaysia, 2019, pp. 1–6.
- [5] F. A. d'Oliveira, F. C. L. d. Melo, and T. C. Devezas, "High-altitude platforms—present situation and technology trends," *Journal of Aerospace Technology and Management*, vol. 8, no. 3, pp. 249–262, 2016.
- [6] Airbus, "Zephyr: The world's leading solar-electric stratospheric unmanned aerial system (UAS)," <https://www.airbus.com/en/products-services/defence/uas/zephyr>, 2024, accessed: May 10, 2025.
- [7] M. Jirousek, M. Peichl, S. Anger, S. Dill, and M. Engel, "Design of a synthetic aperture radar instrument for a high-altitude platform," in *IGARSS 2023 - 2023 IEEE International Geoscience and Remote Sensing Symposium*, Pasadena, CA, USA, 2023, pp. 2045–2048.
- [8] M. Jirousek, M. Peichl, S. Anger, S. Dill, and M. Limbach, "The DLR high altitude platform synthetic aperture radar instrument HAPSAR," in *EUSAR 2024; 15th European Conference on Synthetic Aperture Radar*, Munich, Germany, 2024, pp. 1244–1248.
- [9] W.-Q. Wang and H. Shao, "High altitude platform multichannel SAR for wide-area and staring imaging," *IEEE Aerospace and Electronic Systems Magazine*, vol. 29, no. 5, pp. 12–17, May, 2014.

- [10] A. A. Aragón-Zavala, J. L. Cuevas-Ruiz, and J. A. Delgado-Penín, *High-altitude platforms for wireless communications*. John Wiley & Sons, 2008.
- [11] D. W. Hall, C. D. Fortenbach, E. V. Dimiceli, and R. W. Parks, "A preliminary study of solar powered aircraft and associated power trains," Tech. Rep., 1983.
- [12] O. Abbasi, A. Yadav, H. Yanikomeroglu, N.-D. Đào, G. Senarath, and P. Zhu, "HAPS for 6G networks: Potential use cases, open challenges, and possible solutions," *IEEE Wireless Communications*, vol. 31, no. 3, pp. 324–331, June 2024.
- [13] G. K. Kurt, M. G. Khoshkholgh, S. Alfattani, A. Ibrahim, T. S. Darwish, M. S. Alam, H. Yanikomeroglu, and A. Yongacoglu, "A vision and framework for the high altitude platform station (HAPS) networks of the future," *IEEE Communications Surveys & Tutorials*, vol. 23, no. 2, pp. 729–779, 2021.
- [14] Z. Lou, B. E. Y. Belmekki, and M.-S. Alouini, "Coverage analysis of large-scale HAPS networks using directional beams," *IEEE Transactions on Aerospace and Electronic Systems*, pp. 1–15, 2025.
- [15] S. C. Arum and H. Yanikomeroglu, "Extending coverage and capacity from high altitude platforms with a two-tier cellular architecture," *IEEE Transactions on Mobile Computing*, vol. 23, no. 2, pp. 1942–1953, 2024.
- [16] S. Javed and M.-S. Alouini, "System design and parameter optimization for remote coverage from NOMA-based high-altitude platform stations (HAPS)," *IEEE Transactions on Wireless Communications*, vol. 24, no. 2, pp. 1387–1400, 2025.
- [17] A. Nabi and S. Moh, "Joint offloading decision, user association, and resource allocation in hierarchical aerial computing: Collaboration of UAVs and HAP," *IEEE Transactions on Mobile Computing*, pp. 1–17, 2025.
- [18] W. Wu, W. Feng, Y. Fang, Z. Lin, and X. Lu, "Multi-HAP-assisted computation offloading in space-air-ground-sea integrated network," *IEEE Internet of Things Journal*, pp. 1–1, 2025.
- [19] X. Yu, X. Zhang, Y. Rui, K. Wang, X. Dang, and M. Guizani, "Joint resource allocations for energy consumption optimization in HAPS-Aided MEC-NOMA systems," *IEEE Journal on Selected Areas in Communications*, vol. 42, no. 12, pp. 3632–3646, 2024.
- [20] W. Lu, S. Tu, D. Yan, and Y. Wang, "Performance analysis of EFPK laser communication in terrestrial-HAP-satellite links with MRR array," *IEEE Photonics Technology Letters*, vol. 37, no. 12, pp. 651–654, 2025.
- [21] W. Li, B. Ai, Y. Niu, Z. Han, Z. Zhong, and N. Wang, "High altitude platform beam switching and time slot allocation in high-speed railway communications," *IEEE Transactions on Vehicular Technology*, vol. 74, no. 3, pp. 5217–5222, 2025.
- [22] O. Abbasi, H. Yanikomeroglu, and G. Kaddoum, "Hemispherical antenna array architecture for high-altitude platform stations (HAPS) for uniform capacity provision," *IEEE Transactions on Wireless Communications*, vol. 23, no. 12, pp. 19 489–19 504, 2024.
- [23] O. Ahmed Amodu, R. Nordin, N. Fadzilah Abdullah, S. Adeshina Busari, A. Abu-Samah, I. Otung, M. Ali, and M. Behjati, "Technical advancements toward RIS-assisted NTN-based THz communication for 6g and beyond," *IEEE Access*, vol. 12, pp. 183 153–183 181, 2024.
- [24] E. S. Ahrazoglu, I. Altunbas, and E. Erdogan, "Multi-HAPS THz satellite communication: Error and capacity analyses under IQ imbalance," *IEEE Sensors Journal*, pp. 1–1, 2024.
- [25] Z. Niu, H. Yang, Q. Yao, S. Yin, S. Shen, B. Wei, J. Zhang, and A. V. Vasilakos, "HAP networking enables highly reliable space-air-ground optical interconnect: An integrated network perspective," *IEEE Network*, vol. 39, no. 2, pp. 224–231, 2025.
- [26] M. Salamtmoghadas, A. Mehrabian, and H. Yanikomeroglu, "Energy sustainability in dense radio access networks via high altitude platform stations," *IEEE Networking Letters*, vol. 6, no. 1, pp. 21–25, 2024.
- [27] W. Abderrahim, O. Amin, and B. Shihada, "Data center-enabled high altitude platforms: A green computing alternative," *IEEE Transactions on Mobile Computing*, vol. 23, no. 5, pp. 6149–6162, 2024.
- [28] R. Alghamdi, H. Dahrouj, T. Y. Al-Naffouri, and M.-S. Alouini, "Equitable 6G access service via cloud-enabled HAPS for optimizing hybrid air-ground networks," *IEEE Transactions on Communications*, vol. 72, no. 5, pp. 2959–2973, 2024.
- [29] Z. Ali, Z. Rezki, and M.-S. Alouini, "Optimizing power allocation in HAPS-assisted LEO satellite communications," *IEEE Transactions on Machine Learning in Communications and Networking*, vol. 2, pp. 1661–1677, 2024.
- [30] Y. Wang, C. Zhang, T. Ge, and M. Pan, "Efficient data transmission scheme for massive high altitude platform networks," *IEEE Transactions on Network Science and Engineering*, vol. 11, no. 3, pp. 2837–2848, 2024.
- [31] S. Liu, H. Dahrouj, and M.-S. Alouini, "Joint user association and beamforming in integrated satellite-HAPS-ground networks," *IEEE Transactions on Vehicular Technology*, vol. 73, no. 4, pp. 5162–5178, 2024.
- [32] Z. Lou, B. E. Youcef Belmekki, and M.-S. Alouini, "HAPS in the non-terrestrial network nexus: Prospective architectures and performance insights," *IEEE Wireless Communications*, vol. 30, no. 6, pp. 52–58, 2023.
- [33] A. M. Benaya, M. S. Hassan, M. H. Ismail, and T. Landolsi, "Aerial ISAC: A HAPS-assisted integrated sensing, communications and computing framework for enhanced coverage and security," *IEEE Transactions on Green Communications and Networking*, pp. 1–1, 2025.
- [34] S. B. Son and S. Park, "Hierarchical scheduling for oil spill SAR image detection in space-air-ground integrated networks," *IEEE Transactions on Vehicular Technology*, pp. 1–15, 2025.
- [35] W. Li, B. Ai, Y. Niu, Z. Han, N. Wang, and L. Xiong, "End-to-end scheduling of space-air-ground integrated networks for high-speed railways," *IEEE Transactions on Vehicular Technology*, pp. 1–15, 2025.
- [36] Y. Lin, W. Hong, W. Tan, and Y. Wu, "Extension of range migration algorithm to squint circular SAR imaging," *IEEE Geoscience and Remote Sensing Letters*, vol. 8, no. 4, pp. 651–655, 2011.
- [37] Y. Liao, W.-Q. Wang, and Q. H. Liu, "Two-dimensional spectrum for circular trace scanning SAR based on an implicit function," *IEEE Geoscience and Remote Sensing Letters*, vol. 13, no. 7, pp. 887–891, 2016.
- [38] M. Younis, "Digital beam-forming for high resolution wide swath real and synthetic aperture radar," Ph.D. dissertation, Zugl.: Karlsruhe, Univ., Diss., 2004, 2004.
- [39] A. Currie and M. A. Brown, "Wide-swath SAR," in *IEE Proceedings F (Radar and Signal Processing)*, vol. 139, no. 2. IET, 1992, pp. 122–135.
- [40] M. A. Richards *et al.*, *Fundamentals of radar signal processing*. Mcgraw-hill New York, 2005, vol. 1.
- [41] R. W. Beard and T. W. McLain, *Small unmanned aircraft: Theory and practice*. Princeton university press, 2012.
- [42] R. Austin, *Unmanned aircraft systems: UAVS design, development and deployment*. John Wiley & Sons, 2011.
- [43] S. Javed, M.-S. Alouini, and Z. Ding, "An interdisciplinary approach to optimal communication and flight operation of high-altitude long-endurance platforms," *IEEE Transactions on Aerospace and Electronic Systems*, 2023.
- [44] A. J. Oswald, "Efficient contracts are on the labour demand curve: theory and facts," *Labour Economics*, vol. 1, no. 1, pp. 85–113, 1993.
- [45] R. T. Jones, *The unsteady lift of a wing of finite aspect ratio*, 1940, vol. 681.
- [46] A. Administration and U. S. A. Force, *US standard atmosphere, 1976*. National Oceanic and Atmospheric Administration, 1976, vol. 76, no. 1562.
- [47] I. Reda and A. Andreas, "Solar position algorithm for solar radiation applications," *Solar energy*, vol. 76, no. 5, pp. 577–589, 2004.
- [48] G. S. Aglietti, S. Redi, A. R. Tatnall, and T. Markvart, "Harnessing high-altitude solar power," *IEEE Transactions on Energy Conversion*, vol. 24, no. 2, pp. 442–451, 2009.
- [49] S. P. Boyd and L. Vandenberghe, *Convex optimization*. Cambridge university press, 2004.
- [50] M. Grant and S. Boyd, "CVX: Matlab software for disciplined convex programming, version 2.1," 2014.
- [51] M.-A. Lahmeri, W. Ghanem, C. Knill, and R. Schober, "Trajectory and resource optimization for uav synthetic aperture radar," in *2022 IEEE Globecom Workshops (GC Wkshps)*. IEEE, 2022, pp. 897–903.
- [52] H. Zhang, Y. Lin, F. Teng, S. Feng, and W. Hong, "Holographic SAR volumetric imaging strategy for 3-d imaging with single-pass circular InSAR data," *IEEE Transactions on Geoscience and Remote Sensing*, vol. 61, pp. 1–16, 2023.
- [53] Q. Zhang, J. Sun, Y. Lin, S. Han, Y. Wang, and W. Hong, "Large-scene polar format algorithm for circular SAR subaperture imaging," *IEEE Journal of Selected Topics in Applied Earth Observations and Remote Sensing*, vol. 18, pp. 6336–6349, 2025.